

Energy Dynamics in a Simulation of LAPD Turbulence

Brett Friedman

Updated: May 2, 2012

1 Introduction

It is common practice to study a system's linear stability properties to gain insight into turbulent dynamics. It is often easier to calculate and analyze linear modes and growth rates than to simulate and analyze nonlinear turbulence. However, there are several situations in which linear properties can be misleading in understanding turbulent systems. First, linear studies that neglect stable branches of the linear dispersion relation often miss details of nonlinear dynamics. For example, stable eigenmodes can often impact nonlinear dynamics by providing energy sinks and sometimes energy sources not found on the most unstable linear branch [1, 2, 3, 4, 5, 6, 7, 8, 9, 10]. Stable eigenmodes can shift the energy injection and dissipation ranges, making the turbulent dynamics very different from the Kolmogorov picture of hydrodynamic turbulence [11]. Second, systems with non-normal modes (non-orthogonal eigenvectors) display properties that are unexpected from linear calculations [8, 12]. In fact, systems with non-normal modes even make it difficult to predict dynamics when stable eigenmode branches are included in analyses. Third, linear stability analyses miss crucial nonlinear instability effects, which come in several varieties.

The most obvious variety of a nonlinear instability effect is that of subcritical turbulence in which no linear instabilities exist but turbulence is self-sustained given strong enough finite-amplitude perturbations. Several cases of subcritical plasma instabilities have been shown in the literature [13, 14, 15, 16, 17]. The second variety includes cases in which a particular linear instability is present in a system, but the turbulence is maintained by a nonlinear instability mechanism with different physical origin than the linear instability mechanism. This has been thoroughly explored in tokamak edge simulations in which linear ballooning instability drive is overtaken in the

saturated phase by a nonlinear drift-wave drive [18, 19, 20, 21, 22]. Finally, it is often found that a particular linear instability is enhanced and modified in the saturated phase by a nonlinear instability with a similar mechanism as the linear instability, but which depends on nonlinear wavenumber transfers to increase or cause drive [23, 24].

In order to avoid the pitfalls of relying too heavily on linear stability calculations in forming conclusions on turbulence characteristics, it is useful to diagnose turbulent simulations with energy dynamics analyses. Energy dynamics analyses track energy input into turbulent fluctuations and energy dissipation out of them. They also track conservative energy transfer between different energy types (e.g. from potential to kinetic energy) and between different scales, waves, or eigenmodes of a system. In this study, a previously verified and validated two-fluid Braginskii model of turbulence in the Large Plasma Device (LAPD) is subjected to such an energy dynamics analysis. The result is that a nonlinear instability drives and maintains the turbulence in the steady state saturated phase of the simulation. While a linear resistive drift wave instability resides in the system, the nonlinear drift wave instability dominates when the fluctuation amplitude becomes large enough. The nonlinear instability is identified by its energy growth rate spectrum, which varies significantly from the linear growth rate spectrum.

2 The drift wave model

A Braginskii fluid model [25] is used to simulate drift wave turbulence in LAPD. The evolved variables used in the model are the plasma density, N , the electron fluid parallel velocity $v_{\parallel e}$, the potential vorticity $\varpi = \nabla_{\perp} \cdot (N_0 \nabla_{\perp} \phi)$, and the electron temperature T_e . Cold ions are used, which eliminates ion temperature gradient drive, and sound wave effects are neglected. Details and derivations of the model may be found in previous verification and validation studies [26, 27, 28], although electron temperature fluctuations were not included in those studies.

The equations appear with Bohm normalizations: lengths are normalized to ρ_s , times to ω_{ci}^{-1} , velocities to c_s , densities to the equilibrium peak density, and electron temperatures and potentials to the equilibrium peak electron temperature. The equations are:

$$\partial_t N = -\mathbf{v}_E \cdot \nabla N_0 - N_0 \nabla_{\parallel} v_{\parallel e} + \mu_N \nabla_{\perp}^2 N + S_N + \{\phi, N\}, \quad (1)$$

$$\partial_t v_{\parallel e} = -\frac{m_i}{m_e} \frac{T_{e0}}{N_0} \nabla_{\parallel} N + \frac{m_i}{m_e} \nabla_{\parallel} \phi - \nu_e v_{\parallel e} + \{\phi, v_{\parallel e}\}, \quad (2)$$

$$\partial_t \varpi = -N_0 \nabla_{\parallel} v_{\parallel e} - \nu_{in} \varpi + \mu_{\phi} \nabla_{\perp}^2 \varpi + \{\phi, \varpi\}, \quad (3)$$

$$\begin{aligned} \partial_t T_e = & -\mathbf{v}_E \cdot \nabla T_{e0} - 1.71 \frac{2}{3} T_{e0} \nabla_{\parallel} v_{\parallel e} + \frac{2}{3 N_0} \kappa_{\parallel e} \nabla_{\parallel}^2 T_e \\ & - \frac{2 m_e}{m_i} \nu_e T_e + \mu_T \nabla_{\perp}^2 T_e + S_T + \{\phi, T_e\}. \end{aligned} \quad (4)$$

In these equations, μ_N , μ_T , and μ_{ϕ} are artificial diffusion and viscosity coefficients used for subgrid dissipation. They are large enough to achieve saturation and grid convergence, but small enough to allow for turbulence to develop. The value used in the simulations is 1.5×10^{-3} . The electron collisionality ν_e , ion-neutral collisionality ν_{in} , parallel electron thermal conductivity $\kappa_{\parallel e}$, and mass ratio $\frac{m_i}{m_e}$ are calculated from the experimental parameters. There are two sources of free energy: the density gradient due to the equilibrium density profile N_0 , and the equilibrium electron temperature gradient in T_{e0} , both of which are taken from experimental fits. N_0 and T_{e0} are only functions of the distance from the axis r .

The terms in Poisson brackets are the advective nonlinearities, which are the only nonlinearities used in the simulations. The numerical simulations are fully spatial in all three dimensions (as opposed to spectral) and use cylindrical annular geometry ($12 < r < 40 \text{ cm}$). The simulations use periodic boundary conditions in the axial (z) direction and Dirichlet boundary conditions in the radial (r) direction for the fluctuating quantities.

Simulations also use density and temperature sources (S_n and S_T) in order to keep the equilibrium profiles from relaxing away from their experimental shapes. These sources subtract out the azimuthal averages ($m = 0$ zonal component of the density and temperature fluctuations) at each time step. Zonal flows are allowed to form and evolve. The parallel current, which is often found explicitly in these equations is replaced here by $J_{\parallel} = -N_0 v_{\parallel e}$.

Some basic statistical properties of the density fluctuations of the simulation are shown in Fig. 1 compared to the corresponding results from the

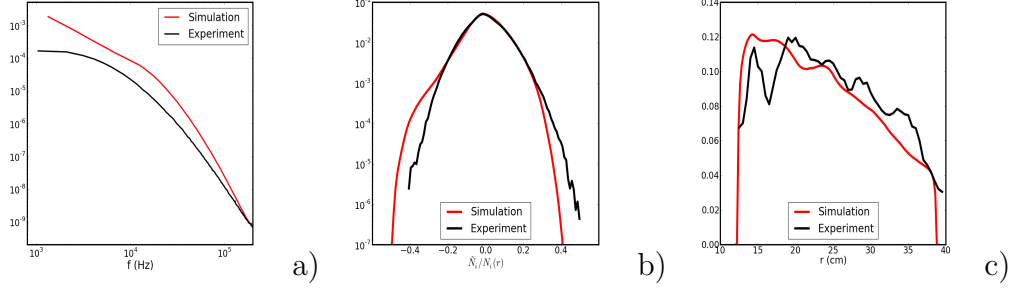


Figure 1: **a)** The power spectral density of the density fluctuations, showing the results from simulation versus experiment, **b)** the probability distribution function of the density fluctuations, and **c)** the RMS amplitude of the density fluctuations as a function of radius.

experiment on which this simulation is based. The simulation reproduces these statistical properties with relatively good qualitative and quantitative accuracy.

3 Energetics Machinery

The expression for the normalized energy of the wave fluctuations in the drift wave model is:

$$E = \frac{1}{2} \int_V (N^2 + \frac{3}{2} T_e^2 + \frac{m_e}{m_i} v_{\parallel e}^2 + N_0 (\nabla_{\perp} \phi)^2) dV. \quad (5)$$

The N^2 contribution is the potential energy due to density fluctuations, $\frac{3}{2} T_e^2$ is the electron temperature fluctuation potential energy, $\frac{m_e}{m_i} v_{\parallel e}^2$ is the parallel electron kinetic energy, and $N_0 (\nabla_{\perp} \phi)^2$ is the $E \times B$ perpendicular kinetic energy. These energies are conserved individually by their respective advective nonlinearities.

It is most instructive to analyze the spectral energy dynamics rather than the total energy dynamics. To do this, each field at a given time is Fourier decomposed as $f(r, \theta, z) = \sum_k f_k(r) e^{i(m\theta + k_z z)}$, where the subscript k represents the spectral wavenumbers, (m, n) . m is the azimuthal wavenumber while n is the axial integer wavenumber such that $k_z = \frac{2\pi n}{l_z}$. Note that the radial direction is not spectrally decomposed because the radial dependence of the

profiles and differential operators complicates the analysis. Then, the energy of each Fourier (m, n) mode is

$$E_{tot}(k) = \frac{1}{2} \left\langle |n_k|^2 + \frac{3}{2} |t_k|^2 + \frac{m_e}{m_i} |v_k|^2 + N_0 \left| \frac{\partial \phi_k}{\partial r} \right|^2 + N_0 \frac{m^2}{r^2} |\phi_k|^2 \right\rangle, \quad (6)$$

where the brackets $\langle \rangle$ represent the radial integral: $\int_{r_a}^{r_b} r dr$. The energy evolution for each Fourier mode of each field has the form:

$$\frac{\partial E_j(k)}{\partial t} = Q_j(k) + C_j(k) + D_j(k) + \sum_{k'} T_j(k, k'). \quad (7)$$

The index j stands for each field, (n, t, v, ϕ) , and the sum over j gives the total energy evolution. The derivation of equation 7 is given in the appendix along with the full expressions for each of the parts. $T_j(k, k')$ is the nonlinear energy transfer function that comes from the advective nonlinearities. It describes the nonlinear energy transfer rate of modes $k' = (m', n')$ and $k - k' = (m - m', n - n')$ to the mode $k = (m, n)$. In other words, a positive value of $T_j(k, k')$ indicates that fluctuations at wavenumber k gain energy from gradient fluctuations at wavenumber k' and flow fluctuations at wavenumber $k - k'$. When summed over k' as in equation 7, the result is the total nonlinear energy transfer into mode k . Note that $\sum_{k, k'} T_j(k, k') = 0$ because the nonlinearities conserve energy individually in each of equations 1-4. This is easily proven by the following identity:

$$\int_{\Omega} q\{p, q\} d\Omega = \int_{\Omega} p\{p, q\} d\Omega = 0, \quad (8)$$

which holds when boundary conditions are periodic or zero value as they are in the simulation. The fact that the advective nonlinearities conserve energy means that they can transfer energy between different Fourier waves, but they cannot change the energy of the volume-averaged fluctuations as a whole. Only the linear terms do this. Other possible nonlinearities that do not conserve energy are not included in the model equation set or in simulations. Furthermore, it is important that the simulations employ an energy conserving finite difference scheme for the advective nonlinearities, and most common numerical advection schemes do not have this property. Therefore, an Arakawa advection scheme that conserves energy of the advected quantity is used for the nonlinear advection terms in the simulations [29].

The linear terms in equations 1-4 do not conserve energy individually or as a whole. The linear terms are broken up into three contributions in equation 7. $D_j(k)$ represents nonconservative energy dissipation due to collisions, artificial diffusion and viscosity, and the purely dissipative density and temperature sources. Each contribution to $D_j(k)$ is negative. $C_j(k)$ contains the linear terms dubbed “transfer channels” [20]. They are rewritten here:

$$C_n(k) = \text{Re} \{ \langle -ik_z N_0 v_k n_k^* \rangle \} \quad (9)$$

$$C_v(k) = \text{Re} \{ \langle -ik_z N_0 n_k v_k^* + ik_z N_0 \phi_k v_k^* - 1.71 ik_z T_{e0} t_k v_k^* \rangle \} \quad (10)$$

$$C_\phi(k) = \text{Re} \{ \langle ik_z N_0 v_k \phi_k^* \rangle \} \quad (11)$$

$$C_t(k) = \text{Re} \{ \langle -1.71 ik_z T_{e0} v_k t_k^* \rangle \} \quad (12)$$

Notice that $C_n(k) + C_v(k) + C_\phi(k) + C_t(k) = 0$, which is most clearly seen upon conjugation of $C_v(k)$ inside the real part operator. This is the reason why these terms are called transfer channels. They represent the transfer between the different types of energy of the different fields ($N, \phi, T_e \leftrightarrow v_{\parallel e}$), but taken together, they do not create or dissipate total energy from the system. The only energy field transfer in this system occurs through the parallel electron velocity (parallel current) dynamics. There is no direct transfer between the state variables N, ϕ , and T_e . Altogether, the coupling through the parallel current is called the adiabatic response. It is an essential part of both the linear and nonlinear drift wave mechanisms [20, 22]. The adiabatic response moves energy from the pressure fluctuations to the perpendicular flow through the parallel current.

Finally, the $Q_j(k)$ terms represent the nonconservative energy sources. They are rewritten here:

$$Q_n(k) = \text{Re} \left\{ \left\langle -\frac{im}{r} \partial_r N_0 \phi_k n_k^* \right\rangle \right\} \quad (13)$$

$$Q_v(k) = \text{Re} \left\{ \left\langle ik_z \frac{N_0^2 - T_{e0}}{N_0} n_k v_k^* + ik_z (1 - N_0) \phi_k v_k^* + 1.71 ik_z (T_{e0} - 1) t_k v_k^* \right\rangle \right\} \quad (15)$$

$$Q_\phi(k) = 0 \quad (16)$$

$$Q_t(k) = \text{Re} \left\{ \left\langle -\frac{3im}{2r} \partial_r T_{e0} \phi_k t_k^* \right\rangle \right\} \quad (17)$$

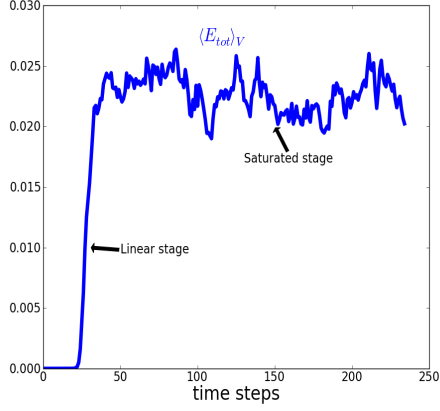


Figure 2: Time evolution of the volume-averaged total energy. Each time step is $400/\omega_{ci} \sim 170\mu s$

$Q_n(k)$ is the energy extraction from the equilibrium density profile. This term may have either sign, so it can dissipate fluctuation potential energy from the system as well as create it at each k . $Q_t(k)$ is completely analogous to $Q_n(k)$. $Q_v(k)$ is parallel kinetic energy extraction or dissipation. The source of these terms are the equilibrium gradients, which is evident because if the profiles were flat ($N_0 = T_{e0} = 1$), all $Q(k)$ would vanish. Moreover, the particular normalization of equations 1-4 combined with the choice of energy definition (equation 5) causes the non-zero $Q_v(k)$.

4 Nonlinear Energy Dynamics

Fig. 2 shows the time evolution of the total energy of the fluctuations. The simulation starts with a random initial perturbation, and the fluctuations grow exponentially until reaching saturation. All analysis of the saturated or turbulent stage is done by averaging over the time steps from 100-235 (the simulation uses tens of thousands of internal time steps for each of these time steps that is output). The turbulent spectral energy, defined in equation 6 is shown in Fig. 3. The energy is broken up into its different types. There are a few clear nonlinear properties seen in these figures. The first is that the energy is located in different spectral regions for the different energy types. This has to be a nonlinear effect because the linear eigenmodes are Fourier

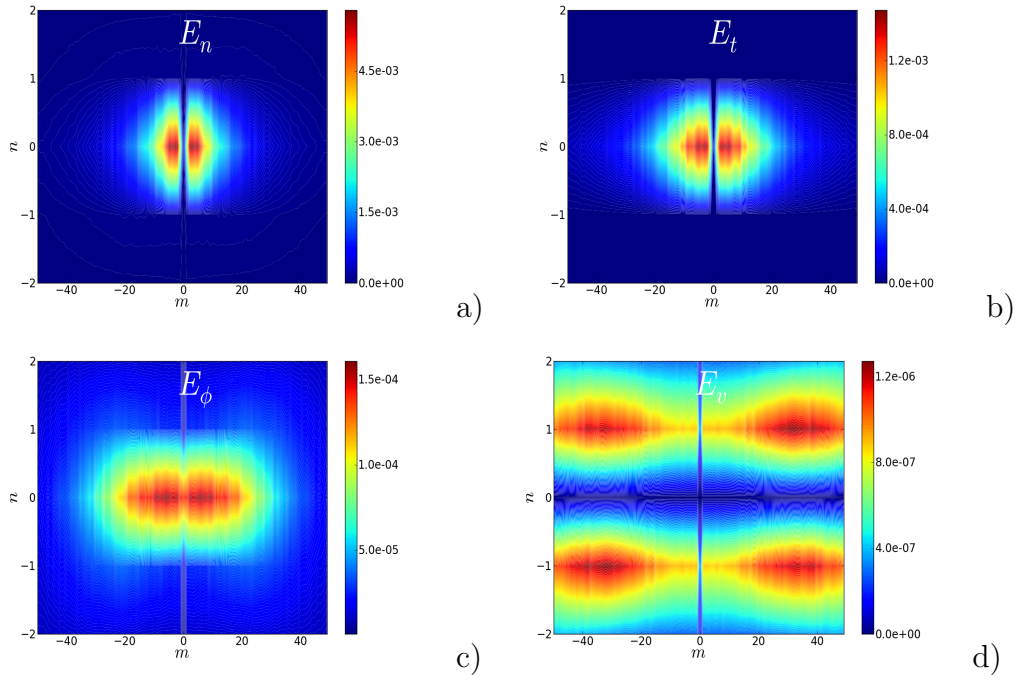


Figure 3: **a)** $E_n(k)$, **b)** $E_t(k)$, **c)** $E_\phi(k)$, and **d)** $E_v(k)$ in the $m - n$ plane averaged over time during the saturated turbulent phase. Note the different scales used on each figure.

modes in the azimuthal and axial directions and all fields grow at the same rate for an eigenmode. Another property unexpected from linear stability analysis is that the majority of the potential energy (E_n and E_t) is contained in $n = 0$ structures, which are often called convective cells. This is unexpected because there is no $n = 0$ linear instability present in the system, which has been confirmed by eigenvalue calculations. The only linear instability of the system is the linear resistive drift wave instability, which requires finite n to provide the phase shift and state variable coupling to drive the waves unstable.

Clearly, the nonlinearities are responsible for these properties. This model is similar to the Hasegawa-Wakatani model ([30]), and it is well-known in the Hasegawa-Wakatani model that the nonlinearities cause a dual cascade in the perpendicular wavenumber. The nonlinearity in the density equation tends to cause a forward cascade while the polarization nonlinearity in the vorticity equation tends to cause an inverse cascade, creating a difference in the shape of the spectra between the density and potential. The coupling between the density and potential works to mitigate this difference, with the difference determined by the strength of the coupling, which is generally measured in terms of the adiabaticity parameter [31].

The $n = 0$ potential energy dominance is also caused by the nonlinearities, but in a complicated way, first described in [23, 15]. The mechanism is best described with help from the energy dynamics machinery derived in section 3. Fig. 4 summarizes the effects of the nonconservative linear terms, which are fully responsible for injecting energy into the fluctuations. Fig. 4a shows the E_n dynamics separated into different parallel wavenumbers and plotted against the azimuthal wavenumber m . Surprisingly, the linear terms inject near equal amounts of energy into $n = 0$ convective cell structures as $n = \pm 1$ structures despite the absence of linear instability at $n = 0$. Modes with $n \geq 2$ play a negligible role. Furthermore, all of the net energy injected into the density fluctuations ($Q_n + D_n$) is transferred out (C_n) to the parallel current (electron velocity), which only occurs at finite n . The net change of E_n is zero because this analysis is averaged over the steady state turbulence. The necessary balance implies, as will be proven later, that the nonlinearities transfer energy from $n = 0$ convective cells to $n = \pm 1$ modes, where that energy can then be transferred to the parallel current. Finally, the dashed curves show the dynamics early on in the linear stage before the

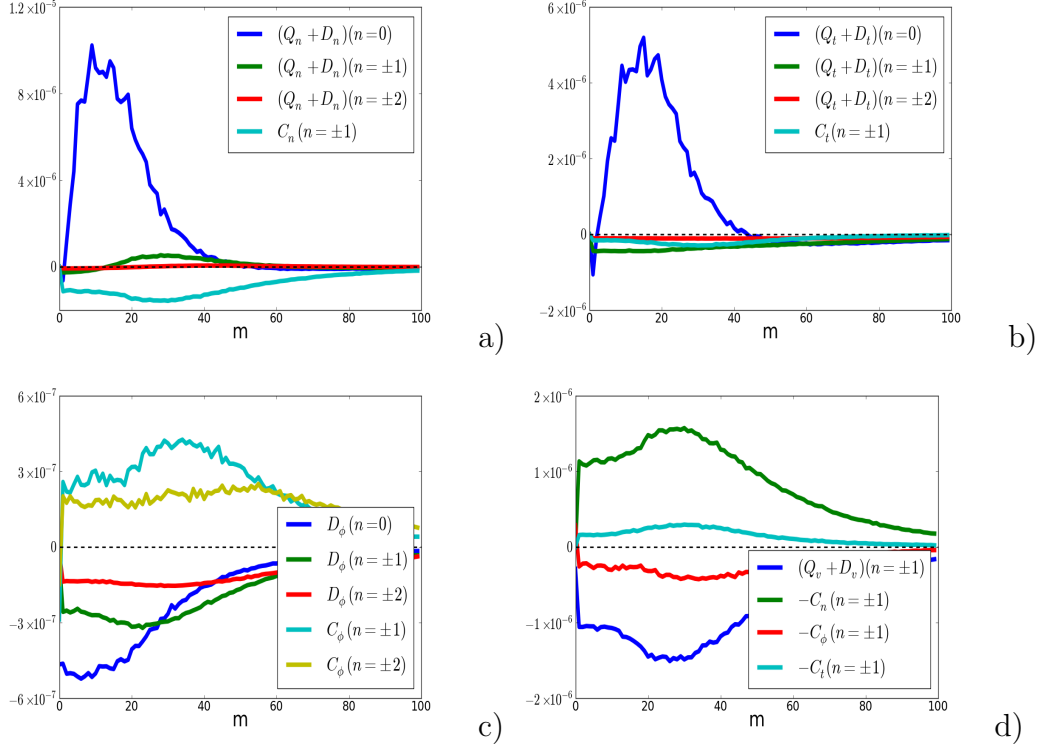


Figure 4: **a)** The solid curves quantify the energy dynamics of the density potential energy averaged over time during the saturated turbulent phase. The notation $n \pm 1$ represents the summation over the $n = 1$ and $n = -1$ curves. **b)** The energy dynamics of the temperature potential energy, **c)** the perpendicular kinetic energy, and **d)** the parallel dynamics (adiabatic response). The contributions to $C_v(k)$ in **d)** are broken up with $C_v(k) = -C_n(k) - C_t(k) - C_\phi(k)$. The density and temperature sources are neglected in **a)** and **b)** respectively. They only contribute at $m = 0$.

nonlinearities make significant contributions. The large difference in the energy injection spectrum between the linear and saturated turbulent phases indicates that the linear instability mechanism is overtaken by a nonlinear instability mechanism.

Fig. 4b shows the temperature potential energy dynamics. Again convective cells inject energy into the fluctuations, but unlike in the density case, $n = \pm 1$ modes dissipate more energy than they inject. Moreover, the small value of C_t reveals that the temperature fluctuations inject only a small amount of energy into the parallel current compared to the density fluctuations. Despite the fact that the equilibrium temperature gradient is quite a bit steeper than the density gradient, its free energy is not used efficiently by the waves in the sense that it is largely dissipated before being transferred to the electrostatic potential. The reason for the difference between the density and temperature responses is the extra dissipation routes for the temperature fluctuations, namely, the parallel heat conduction and electron-ion heat exchange. One should therefore be careful in assuming that adding free energy sources to an analysis will automatically increase instability drive. The same type of result was seen in a study of tokamak edge turbulence [19], although there, the temperature fluctuations were even more dissipative than in this study in that they actually drew energy from the parallel current.

Next, Fig. 4c illustrates the perpendicular kinetic energy dynamics provided by the electrostatic potential ϕ . Since there is no free energy source for the potential ($Q_\phi = 0$), the potential fluctuations derive their energy from the parallel current through the C_ϕ transfer channel, which is positive everywhere and only finite for finite n . Otherwise, ion-neutral collisions and viscosity dissipate energy from the potential fluctuations as shown by the D_ϕ curves.

The last piece, the parallel dynamics, also called the adiabatic response, is displayed in Fig. 4d. The primary effect of the adiabatic response is to take energy from the density fluctuations and transfer it to the potential fluctuations, which only occurs at finite parallel wavenumber. Resistivity dissipates a fair portion of this energy, and in the linear regime, provides the primary phase shift mechanism between the density and potential that allows for instability. The temperature fluctuations also provide energy to the potential fluctuations through this response, although it is much weaker than the density fluctuation route.

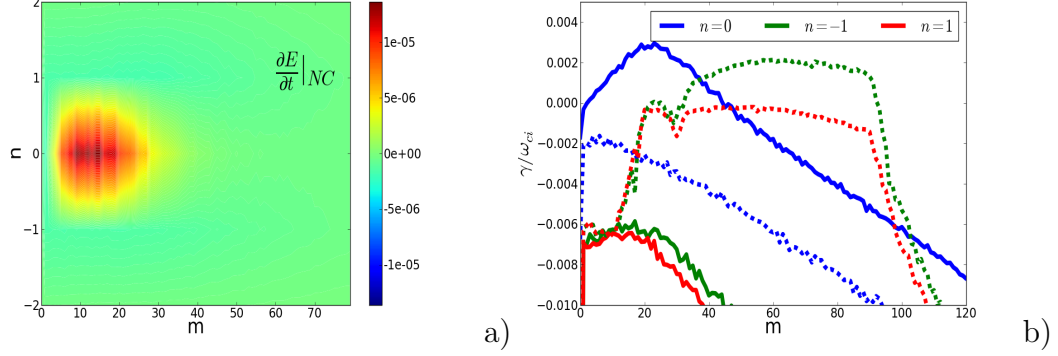


Figure 5: **a)** The total spectral nonconservative energy injection $\frac{\partial E(k)}{\partial t}|_{nl} = \sum_j Q_j(k) + C_j(k) + D_j(k)$ and **b)** the spectral nonconservative growth rate spectrum $\gamma(k)_{nl} = [\sum_j Q_j(k) + C_j(k) + D_j(k)]/[2\sum_j E_j(k)]$ averaged over the saturated phase compared to the linear growth rate spectrum (γ_L). The solid lines represent $\gamma(k)_{nl}$ which is calculated using the saturated turbulent phase, while the dashed lines represent γ_L and are calculated using the linear phase of the simulation.

Finally, Fig. 5 shows the total spectral nonconservative energy rate of change in the turbulent state. Fig. 5a reveals a global picture in wavenumber space of where the total energy is injected into the system and where it is dissipated. Namely, energy is primarily injected at $(n = 0, 10 < m < 60)$, while it is dissipated at $(n = 0, m < 5)$ and at $n = \pm 1$ for all m . This is quite different than what one would expect from the standard hydrodynamic instability picture in which energy is injected where the linear growth rate is positive and dissipated where it is negative. To clarify this point, the linear $\gamma(k)_L$ versus nonlinear growth rate $\gamma(k)_{nl}$ spectra are shown in Fig. 5b. Note that the linear growth rate is positive for $(n = -1, 30 < m < 100)$ and negative everywhere else. Seemingly, the linear physics is completely washed out in the turbulent state.

Although the nonconservative linear term analysis is primary in revealing the energy injection and dissipation routes of the turbulence, the conservative nonlinear transfer analysis completes the picture of energy dynamics.

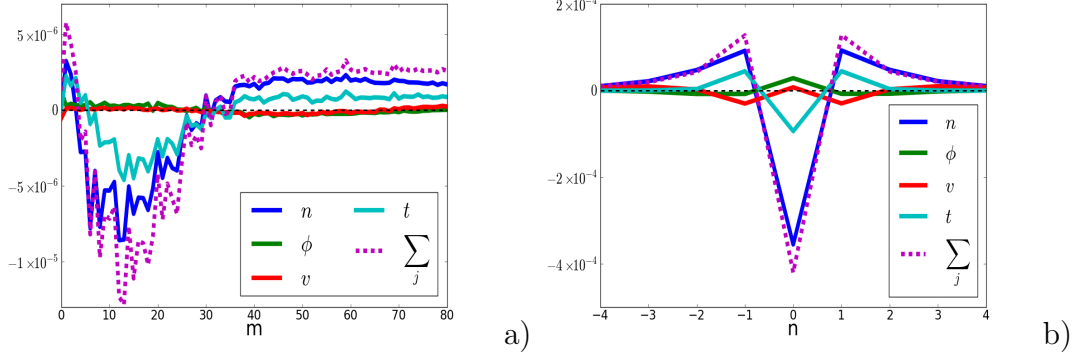


Figure 6: **a)** Conservative nonlinear energy transfer functions $T_j(k, k')$ summed over k' and n . The line labeled ϕ represents the function $\sum_{k', n} T_\phi(k, k')$, which is a function of m . Positive values indicate energy transfer into structures with azimuthal mode number m . **b)** Transfer functions summed over k' and m . Note that $T_v(k, k')$ is multiplied by 20 in both figures to make it visible.

The difficulty in looking at the nonlinear transfer functions ($T_j(k, k')$ in equation 7) is that they are four dimensional functions (m, n, n', m'), which makes complete visualization impossible. It is therefore convenient to sum over various transfers or look at specific wavenumber transfers of interest. The most easily decipherable results that compliment the results of Fig. 4 are shown in Fig. 6. First, Fig. 6a illustrates the azimuthal mode number conservative wavenumber transfers. Note that the sum of each individual curve over m is zero because the nonlinearities are conservative. The density and temperature nonlinearities are qualitatively similar in that they cause both forward and inverse transfer out of the wavenumbers that inject the most energy. The potential (polarization) and parallel velocity nonlinearities cause inverse transfer to low wavenumbers.

Fig. 6b displays the conservative transfers into and out of different parallel modes. As expected from Fig. 4b, density potential energy is transferred from $n = 0$ convective cells into $n \neq 0$ modes. This can be called a direct transfer in analogy with the terminology used for perpendicular wavenumber transfer. The temperature fluctuations have the same transfer tendency as

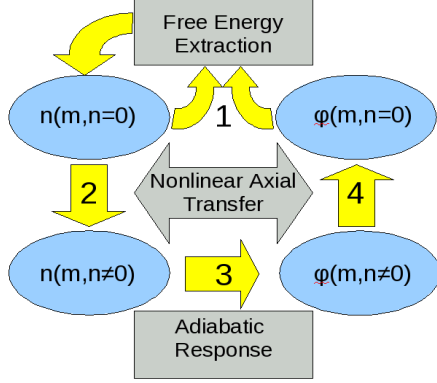


Figure 7: Diagram of the nonlinear instability process that drives convective cells.

the density fluctuations, while the parallel velocity exhibits direct transfer, although from $n = 1$ to higher modes since there is never any $n = 0$ energy in the parallel velocity. The potential fluctuations, on the other hand, exhibit inverse parallel wavenumber transfer, populating $n = 0$ potential structures. This nonlinear transfer is the only way to drive energy into $n = 0$ potential structures because $Q_\phi = 0$. Furthermore, this inverse transfer is necessary to drive the convective cells because $Q_n(m, n = 0)$ and $Q_t(m, n = 0)$ require finite $\phi_{m,n=0}$.

It is now clear that the convective cells draw their energy from a multi-step nonlinear process. Fig. 7 outlines the crucial steps in the process. First, the $n = 0$ density and potential fluctuations nonconservatively draw energy from the equilibrium density gradient as prescribed by $Q_n(m, n = 0)$ defined in equation 13, and feed this energy into the $n = 0$ density fluctuations only. Second, this convective cell energy is conservatively transferred to $n \neq 0$ density fluctuations by the nonlinear $T_n(k, k')$ transfer process. The third step involves the transfer at finite n from the density fluctuations to the potential fluctuations by way of the parallel current in the adiabatic response. Fourth and finally, the $T_\phi(k, k')$ interaction conservatively transfers energy from $n \neq 0$ to $n = 0$ potential $\phi_{m,n=0}$ fluctuations in inverse fashion, at which point the process starts over. This is a clear case of a nonlinear instability as convective cells are nonconservatively fed by a process that relies on the nonlinearities since the linearities alone cannot do this. This shows that linear

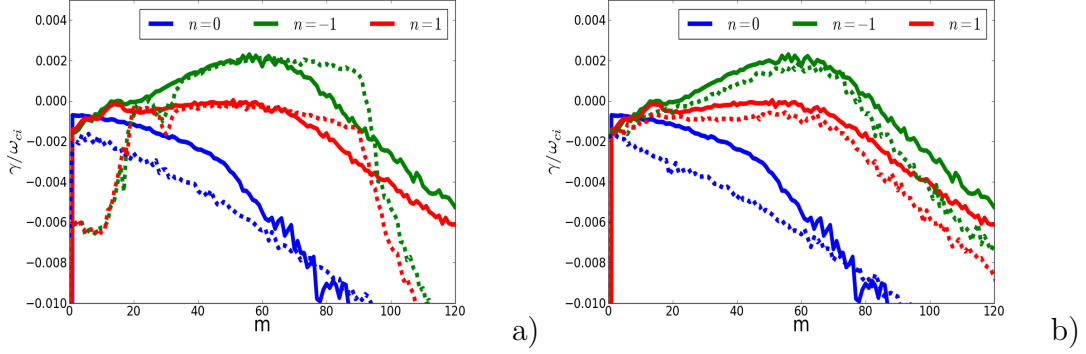


Figure 8: **a)** The nonlinear growth rate spectrum $\gamma(k)_{nl}$ with $n = 0$ density and potential components removed from the simulation compared to the linear growth rate spectrum $\gamma(k)_L$. **b)** The solid lines are the same $\gamma(k)_{nl}$ spectrum as the solid lines in (a), but the dashed lines are the nonlinear growth rate spectrum when the zonal flows are retained in the simulation.

instabilities need not be completely absent for a system to display nonlinear instability.

5 Linear vs nonlinear drive

Although the nonlinear convective cell dynamics present a clear case of nonlinear instability, the $n \neq 0 \leftrightarrow n = 0$ energy path is not a necessary feature of nonlinear drift wave instabilities, which is clear in tokamak studies of drift wave turbulence [18, 19, 20, 21, 22]. Furthermore, the periodic axial boundary conditions used in the LAPD turbulence simulation which allow for axial Fourier eigenmodes (including those with $n = 0$) are obviously unphysical. Eliminating the convective cells is then instructive in determining how robust the nonlinear instability is in this instance of drift wave turbulence. There are a few ways to eliminate the convective cells in the simulation such as eliminating one of the nonlinearities that is essential to the nonlinear instability process described in Fig. 7. However, simply subtracting out the $n = 0$ components of the density and potential at each simulation time step retains more of the physics that may be essential to cause nonlinear instability. The

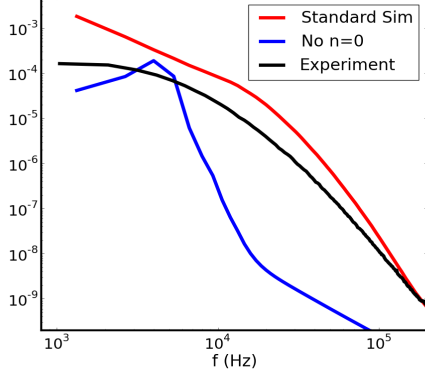


Figure 9: Comparison of the frequency spectra. Notice the spectra with $n = 0$ components removed is not broadband, but has a clear peak, which is inconsistent with experiment.

results of such a simulation are shown in Fig. 8. Interestingly, the nonlinear growth rate spectrum $\gamma(k)_{nl}$ is nearly identical to the linear growth rate spectrum $\gamma(k)_L$, as seen in Fig. 8a. It is noted that subtracting out the $n = 0$ potential component removes the zonal flow ($m = n = 0$) from the system, providing a possible explanation for the large change in behavior of the nonlinear growth rate spectrum. However, this hypothesis is dispelled by the analysis of a simulation in which only the $n = 0, m \neq 0$ potential components are removed while the zonal flow is left intact. The growth rate spectrum of this simulation, shown in Fig. 8b, reveals that the zonal flow plays a minimal role in the nonlinear instability dynamics. The zonal flow simply decreases the growth rates by a small amount, causing no change to the qualitative picture. Therefore, the finite m convective cells or at least an axial wavenumber transfer is necessary for a nonlinear instability to overtake the linear instability in driving the turbulence.

One indication that the nonlinear instability is important is that the turbulence of the simulation with the $n = 0$ components removed becomes more coherent. This can be seen in the wavenumber or frequency spectrum. The frequency spectrum is shown in Fig. 9 compared with the experimental spectra and the spectra of the standard nonlinear instability dominated simulation. The clear peak in the spectra of the $n = 0$ removed simulation

is inconsistent with experiment, indicating that something in the standard simulation – possibly the nonlinear instability – is important for reproducing experimentally relevant turbulence.

A Explicit Calculation of the Energy Evolution of a Fourier Mode

The energy evolution for each Fourier wave mode can be obtained by Fourier decomposing each of equations 1 - 4 and then multiplying the density, electron parallel velocity, vorticity, and electron temperature equations by the complex conjugates of the density, velocity, potential, and temperature respectively, and integrating over space. Adding the resulting equations gives the energy evolution of each Fourier mode.

Take the density equation as an example for this procedure. The decomposition for the density is:

$$N(r, \theta, z, t) = \sum_k n_k(r, t) e^{i(m\theta + k_z z)}. \quad (18)$$

Recall that the subscript k is short for (m, n) as the decomposition is a 2D Fourier decomposition in the azimuthal and axial directions, making the sum over k truly a double sum over m and n . Furthermore, positive and negative m and n are included in the sums to ensure reality of N , which also requires that $n_{-k} = n_k^*$. Similar decompositions are used for $v_{\parallel e}$ and ϕ . The density source is azimuthally symmetric, so it is decomposed as:

$$S_N(r, z, t) = \sum_{k_z} S_{N_{k_z}}(r, t) e^{ik_z z}. \quad (19)$$

Substituting this decomposition into equation 1 gives:

$$\begin{aligned} \sum_k \frac{\partial n_k}{\partial t} e^{i(m\theta + k_z z)} &= \sum_{k_z} S_{N_{k_z}} e^{ik_z z} + \\ \sum_k \left[-\frac{im}{r} \partial_r N_0 \phi_k - ik N_0 v_k + \mu_N (\partial_r^2 n_k + \frac{1}{r} \partial_r n_k - \frac{m^2}{r^2} n_k) \right] e^{i(m\theta + k_z z)} \\ &+ \frac{1}{r} \sum_{k, k'} (im n_k \partial_r \phi_{k'} - im' \partial_r n_k \phi_{k'}) e^{i(m+m')\theta + i(k_z + k'_z)z}. \end{aligned} \quad (20)$$

Multiplying through by $n_{k''}^* e^{-im''\theta - ik_z''z}$ and integrating over space (and permuting primes) gives:

$$\begin{aligned} \left\langle \frac{\partial n_k}{\partial t} n_k^* \right\rangle &= \left\langle S_{Nk_z} n_{m=0,k_z}^* \right\rangle \\ \left\langle -\frac{im}{r} \partial_r N_0 \phi_k n_k^* - ik N_0 v_k n_k^* + \mu_N (\partial_r^2 n_k + \frac{1}{r} \partial_r n_k - \frac{m^2}{r^2} n_k) n_k^* \right\rangle \\ &+ \left\langle \frac{1}{r} \sum_{k'} (im' n_{k'} \partial_r \phi_{k-k'} n_k^* - i(m-m') \partial_r n_{k'} \phi_{k-k'} n_k^*) \right\rangle. \end{aligned} \quad (21)$$

Finally, taking the real part of this equation results in:

$$\begin{aligned} \left\langle \frac{1}{2} \frac{\partial |n_k|^2}{\partial t} \right\rangle &= Re \left\{ \left\langle S_{Nk_z} n_{m=0,k_z}^* \right\rangle \right\} \\ Re \left\{ \left\langle -\frac{im}{r} \partial_r N_0 \phi_k n_k^* - ik N_0 v_k n_k^* + \mu_N (\partial_r^2 n_k + \frac{1}{r} \partial_r n_k - \frac{m^2}{r^2} n_k) n_k^* \right\rangle \right\} \\ &+ Re \left\{ \left\langle \frac{1}{r} \sum_{k'} (im' n_{k'} \partial_r \phi_{k-k'} n_k^* - i(m-m') \partial_r n_{k'} \phi_{k-k'} n_k^*) \right\rangle \right\}. \end{aligned} \quad (22)$$

Note that taking the real part of the equation produces the expected energy-like term on the left hand side because:

$$\frac{1}{2} \frac{\partial |n_k|^2}{\partial t} = Re \left\{ \frac{\partial n_k}{\partial t} n_k^* \right\}. \quad (23)$$

Breaking the result into explicit parts:

$$\frac{\partial E_n(k)}{\partial t} = Q_n(k) + C_n(k) + D_n(k) + \sum_{k'} T_n(k, k') \quad (24)$$

$$E_n(k) = \frac{1}{2} \langle |n_k|^2 \rangle \quad (25)$$

$$Q_n(k) = Re \left\{ \left\langle -\frac{im}{r} \partial_r N_0 \phi_k n_k^* \right\rangle \right\} \quad (26)$$

$$C_n(k) = Re \left\{ \langle -ik N_0 v_k n_k^* \rangle \right\} \quad (27)$$

$$D_n(k) = Re \left\{ \left\langle \mu_N (\partial_r^2 n_k + \frac{1}{r} \partial_r n_k - \frac{m^2}{r^2} n_k) n_k^* + S_{Nk_z} n_{m=0,k_z}^* \right\rangle \right\} \quad (28)$$

$$T_n(k, k') = Re \left\{ \left\langle \frac{1}{r} (im' n_{k'} \partial_r \phi_{k-k'} n_k^* - i(m-m') \partial_r n_{k'} \phi_{k-k'} n_k^*) \right\rangle \right\} \quad (29)$$

$Q_n(k)$ is the source, $C_n(k)$ is the transfer channel, $D_n(k)$ is dissipation, and $T_n(k, k')$ is spectral energy transfer. The same type of procedure may be applied to equations 2-4. However, the double primed conjugate multiplications (as in the step between equations 20 and 21) must be done with the Fourier fields, $\frac{m_e}{m_i}v_{k''}$, $-\phi_{k''}$, and $\frac{3}{2}t_{k''}$ rather than $v_{k''}$, $\varpi_{k''}$, and $t_{k''}$. These produce the correct energy terms, and most importantly still conserve the nonlinearities. The corresponding expressions for the perpendicular kinetic energy are:

$$\frac{\partial E_\phi(k)}{\partial t} = Q_\phi(k) + C_\phi(k) + D_\phi(k) + \sum_{k'} T_\phi(k, k') \quad (30)$$

$$E_\phi(k) = \frac{1}{2} \left\langle N_0 \left| \frac{\partial \phi_k}{\partial r} \right|^2 + N_0 \frac{m^2}{r^2} |\phi_k|^2 \right\rangle \quad (31)$$

$$Q_\phi(k) = 0 \quad (32)$$

$$C_\phi(k) = Re \{ \langle i k_z N_0 v_k \phi_k^* \rangle \} \quad (33)$$

$$D_\phi(k) = Re \left\{ \left\langle -\mu_\phi (\partial_r^2 \varpi_k + \frac{1}{r} \partial_r \varpi_k - \frac{m^2}{r^2} \varpi_k) \phi_k^* - \nu_{in} E_\phi(k) \right\rangle \right\} \quad (34)$$

$$T_\phi(k, k') = Re \left\{ \left\langle -\frac{1}{r} (i m' \varpi_{k'} \partial_r \phi_{k-k'} \phi_k^* - i(m - m') \partial_r \varpi_{k'} \phi_{k-k'} \phi_k^*) \right\rangle \right\} \quad (35)$$

and for the electron temperature potential energy:

$$\frac{\partial E_t(k)}{\partial t} = Q_t(k) + C_t(k) + D_t(k) + \sum_{k'} T_t(k, k') \quad (36)$$

$$E_t(k) = \frac{3}{4} \langle |t_k|^2 \rangle \quad (37)$$

$$Q_t(k) = Re \left\{ \left\langle -\frac{3}{2} \frac{i m}{r} \partial_r T_{e0} \phi_k t_k^* \right\rangle \right\} \quad (38)$$

$$C_t(k) = Re \{ \langle -1.71 i k_z T_{e0} v_k t_k^* \rangle \} \quad (39)$$

$$D_t(k) = Re \left\{ \left\langle -\frac{\kappa_{||e}}{N_0} k_z^2 |t_k|^2 - \frac{3 m_e}{m_i} \nu_e |t_k|^2 + \frac{3}{2} \mu_T (\partial_r^2 t_k + \frac{1}{r} \partial_r t_k - \frac{m^2}{r^2} t_k) t_k^* + \frac{3}{2} S_{Tk_z} t_{m=0, k_z}^* \right\rangle \right\} \quad (40)$$

$$T_t(k, k') = Re \left\{ \left\langle \frac{3}{2r} (i m' t_{k'} \partial_r \phi_{k-k'} t_k^* - i(m - m') \partial_r t_{k'} \phi_{k-k'} t_k^*) \right\rangle \right\} \quad (41)$$

and for the parallel kinetic energy:

$$\frac{\partial E_v(k)}{\partial t} = Q_v(k) + C_v(k) + D_v(k) + \sum_{k'} T_v(k, k') \quad (42)$$

$$E_v(k) = \frac{1}{2} \frac{m_e}{m_i} \langle |v_k|^2 \rangle \quad (43)$$

$$Q_v(k) = Re \left\{ \left\langle ik_z \frac{N_0^2 - T_{e0}}{N_0} n_k v_k^* + ik_z (1 - N_0) \phi_k v_k^* + 1.71 ik_z (T_{e0} - 1) t_k v_k^* \right\rangle \right\} \quad (44)$$

$$C_v(k) = Re \{ \langle -ik_z N_0 n_k v_k^* + ik_z N_0 \phi_k v_k^* - 1.71 ik_z T_{e0} t_k v_k^* \rangle \} \quad (45)$$

$$D_v(k) = Re \left\{ \left\langle -\nu_e \frac{m_e}{m_i} |v_k|^2 \right\rangle \right\} \quad (46)$$

$$T_v(k, k') = Re \left\{ \frac{m_e}{m_i} \left\langle \frac{1}{r} (im' v_{k'} \partial_r \phi_{k-k'} v_k^* - i(m - m') \partial_r v_{k'} \phi_{k-k'} v_k^*) \right\rangle \right\} \quad (47)$$

The transfer channel $C_v(k)$ is specifically set so that $C_n(k) + C_t(k) + C_\phi(k) + C_v(k) = 0$. The source $Q_v(k)$ is the left over quantity, which can have any sign and contributes to the overall energy evolution.

References

- [1] D.A. Baver, P.W. Terry, R. Gatto, and Eduardo Fernandez. Nonlinear stability and instability in collisionless trapped electron mode turbulence. *Phys. Plasmas*, 9:3318, 2002.
- [2] P.W. Terry, R. Gatto, and D.A. Baver. Nonlinear damping of plasma zonal flows excited by inverse spectral transfer. *Phys. Rev. Lett.*, 89:205001, 2002.
- [3] P.W. Terry and R. Gatto. Nonlinear inward particle flux component in trapped electron mode turbulence. *Phys. Plasmas*, 13:062309, 2006.
- [4] P.W. Terry, D.A. Baver, and Sangeeta Gupta. Role of stable eigenmodes in saturated local plasma turbulence. *Phys. Plasmas*, 13:022307, 2006.
- [5] R. Gatto, P.W. Terry, and D.A. Baver. Nonlinear damping of zonal modes in anisotropic weakly collisional trapped electron mode turbulence. *Phys. Plasmas*, 13:022306, 2006.
- [6] P.W. Terry, D.A. Baver, and D.R. Hatch. Reduction of inward momentum flux by damped eigenmodes. *Phys. Plasmas*, 16:122305, 2009.

- [7] D.R. Hatch, P.W. Terry, W.M. Nevins, and W. Dorland. Role of stable eigenmodes in gyrokinetic models of ion temperature gradient turbulence. *Phys. Plasmas*, 16:022311, 2009.
- [8] J.-H. Kim and P.W. Terry. Energetic study of the transition to nonlinear state in two-dimensional electron temperature gradient fluid turbulence. *Phys. Plasmas*, 17:112306, 2010.
- [9] K.D. Makwana, P.W. Terry, J.-H. Kim, and D.R. Hatch. Damped eigenmode saturation in plasma fluid turbulence. *Phys. Plasmas*, 18:012302, 2011.
- [10] D.R. Hatch, P.W. Terry, F. Jenko, F. Merz, and W.M. Nevins. Saturation of gyrokinetic turbulence through damped eigenmodes. *Phys. Rev. Lett.*, 106:115003, 2011.
- [11] A. N. Kolmogorov. The local structure of turbulence in incompressible viscous fluid for very large reynolds numbers. *Dokl Akad. Nauk SSSR*, 30:301–305, 1941.
- [12] S.J. Camargo, M.K. Tippet, and I.L. Caldas. Nonmodal energetics of resistive drift waves. *Phys. Rev. E*, 58:3693, 1998.
- [13] B. D. Scott. Self-sustained collisional drift-wave turbulence in a sheared magnetic field. *Phys. Rev. Lett.*, 65:3289, 1990.
- [14] B. D. Scott. The mechanism of self sustainment in collisional drift wave turbulence. *Phys. Fluids B*, 4:2468, 1992.
- [15] J.F. Drake, A. Zeiler, and D. Biskamp. Nonlinear self-sustained drift-wave turbulence. *Phys. Rev. Lett.*, 75:4222, 1995.
- [16] H. Nordman, V.P. Pavlenko, and J. Weiland. Subcritical reactive drift wave turbulence. *Phys. Fluids B*, 5:402, 1993.
- [17] R.E. Waltz. Subcritical magnetohydrodynamic turbulence. *Phys. Rev. Lett.*, 55:1098, 1985.
- [18] A. Zeiler, D. Biskamp, J.F. Drake, and P.N. Guzdar. Three-dimensional fluid simulations of tokamak edge turbulence. *Phys. Plasmas*, 3:2951, 1996.

- [19] A. Zeiler, J.F. Drake, and D. Biskamp. Electron temperature fluctuations in drift-resistive ballooning turbulence. *Phys. Plasmas*, 4:991, 1997.
- [20] B. D. Scott. The nonlinear drift wave instability and its role in tokamak edge turbulence. *New J. Physics*, 4:52.1–52.30, 2002.
- [21] B. D. Scott. Computation of electromagnetic turbulence and anomalous transport mechanisms in tokamak plasmas. *Plasma Phys. Control. Fusion*, 45:A385–A398, 2003.
- [22] B. D. Scott. Drift wave versus interchange turbulence in tokamak geometry: Linear versus nonlinear mode structure. *Phys. Plasmas*, 12:062314, 2005.
- [23] D. Biskamp and A. Zeiler. Nonlinear instability mechanism in 3d collisional drift-wave turbulence. *Phys. Rev. Lett.*, 74:706, 1995.
- [24] S. B. Korsholm, P. K. Michelsen, and V. Naulin. Resistive drift wave turbulence in a three-dimensional geometry. *Phys. Plasmas*, 6:2401, 1999.
- [25] S I Braginskii. Transport processes in a plasma. In M A Leontovich, editor, *Reviews of Plasma Physics*, volume 1, pages 205–311. Consultants Bureau, New York, 1965.
- [26] P. Popovich, M.V. Umansky, T. A. Carter, and B. Friedman. Analysis of plasma instabilities and verification of bout code for linear plasma device. *Phys. Plasmas*, 17:102107, 2010.
- [27] P. Popovich, M.V. Umansky, T. A. Carter, and B. Friedman. Modeling of plasma turbulence and transport in the large plasma device. *Phys. Plasmas*, 17:122312, 2010.
- [28] M.V. Umansky, P. Popovich, T. A. Carter, B. Friedman, and W.M. Nevins. Numerical simulation and analysis of plasma turbulence the large plasma device. *Phys. Plasmas*, 18:055709, 2011.
- [29] A. Arakawa. Computational design for long-term numerical integration of the equations of fluid motion. *J. Computational Physics*, 1:119–143, 1966.

- [30] A. Hasegawa and M. Wakatani. Plasma edge turbulence. *Phys. Rev. Lett.*, 50:682–686, 1983.
- [31] S.J. Camargo, D. Biskamp, and B.D. Scott. Resistive drift-wave turbulence. *Phys. Plasmas*, 2:48, 1995.